



Influence of spin fluctuations on structural phase transitions of iron

Ning Wang,¹ Thomas Hammerschmidt ¹, Tilmann Hickel ^{2,3}, Jutta Rogal ^{4,5} and Ralf Drautz ¹

¹*ICAMS, Ruhr-Universität Bochum, Universitätsstrasse 150, 44801 Bochum, Germany*

²*Max-Planck-Institut für Eisenforschung GmbH, Max-Planck-Strasse 1, 40237 Düsseldorf, Germany*

³*BAM Federal Institute for Materials Research and Testing, Richard-Willstätter-Str. 11, 12489 Berlin, Germany*

⁴*Department of Chemistry, New York University, New York, 10003, USA*

⁵*Fachbereich Physik, Freie Universität Berlin, 14195 Berlin, Germany*



(Received 2 December 2021; revised 12 August 2022; accepted 5 January 2023; published 29 March 2023)

The effect of spin fluctuations on the α (bcc)- γ (fcc)- δ (bcc) structural phase transitions in iron is investigated with a tight-binding (TB) model. The orthogonal d -valent TB model is combined with thermodynamic integration, spin-space averaging, and Hamiltonian Monte Carlo to compute the temperature-dependent free-energy difference between bcc and fcc iron. We demonstrate that the TB model captures experimentally observed phonon spectra of bcc iron at elevated temperatures. Our calculations show that spin fluctuations are crucial for both the α - γ and γ - δ phase transitions but they enter through different mechanisms. Spin fluctuations impact the α - γ phase transition mainly via the magnetic/electronic free-energy difference between bcc and fcc iron. The γ - δ phase transition, in contrast, is influenced by spin fluctuations only indirectly via the spin-lattice coupling. Combining the two mechanisms, we obtain both the α - γ and γ - δ phase transitions with our TB model. The calculated transition temperatures are in very good agreement with experimental values.

DOI: [10.1103/PhysRevB.107.104108](https://doi.org/10.1103/PhysRevB.107.104108)

I. INTRODUCTION

Iron exhibits a rich and complex phase diagram with several structural and magnetic phase transitions. The magnetism of iron originates from the spin angular momentum of the electrons. The effect of spin fluctuations on structural phase transitions in iron, the focus of this paper, has been investigated with a variety of theoretical methods, but a complete understanding of the microscopic origin of the structural phase transitions is still missing.

Hasegawa and Pettifor [1] were probably the first to give a systematic investigation of the spin-fluctuation effect on the phase diagram of iron. One of their main conclusions is that spin fluctuations lead to different changes in magnetic free energies with temperature in bcc and fcc iron and thus drive the α (bcc)- γ (fcc)- δ (bcc) phase transitions of iron. As their calculations were based on a single-band tight-binding model and the coherent potential approximation, their results can be interpreted only qualitatively. Indeed, their argument that the spin fluctuations alone drive the γ (fcc)- δ (bcc) phase transition is not supported by recent more accurate calculations [2] with density-functional theory (DFT) combined with dynamical mean-field theory (DMFT). According to this work, the magnetic free-energy contribution is responsible for the α (bcc)- γ (fcc) but not the γ (fcc)- δ (bcc) phase transition. As the spin fluctuations alone cannot give a consistent explanation of α - γ - δ phase transitions, researchers included the effect of atomic vibrations by also considering the vibrational free energy. Confusingly, different methods give qualitatively different conclusions regarding the effect of atomic vibrations on the phase transitions in iron. For example, DFT-based phonon

calculations showed that atomic vibrations tend to stabilize fcc iron [3], while spin-lattice dynamics based on classical interatomic potentials suggest that atomic vibrations tend to stabilize bcc iron [4]. In fact, the atomic vibrations themselves are strongly impacted by spin fluctuations [5–7] and cannot be treated independently, which makes the dynamic spin-lattice coupling a crucial factor for phase transitions of iron.

In this work, we compare the relative stability of bcc and fcc iron in terms of the temperature-dependent free-energy difference

$$\Delta F(T) = F_{\text{fcc}}(T) - F_{\text{bcc}}(T). \quad (1)$$

We compute the contributions to the free-energy difference as a sum of two contributions,

$$\Delta F(T) = \Delta F^{\text{elec}}(T) + \Delta F^{\text{vib}}(T). \quad (2)$$

The magnetic/electronic contribution ΔF^{elec} takes into account spin fluctuations. The vibrational contribution ΔF^{vib} is also strongly influenced by spin fluctuations through the dependence of atomic forces on magnetism [5–9]. Here, we compute both contributions to the free-energy difference in the framework of an orthogonal d -valent tight-binding (TB) model. We demonstrate that this physically transparent and approximate treatment of the electronic structure is sufficient to reveal the influence of spin fluctuations on both structural phase transitions of iron. Within our approach we present a comprehensive framework that captures both the α - γ and γ - δ transitions on the same footing. Unlike previous approaches, our framework provides a microscopic understanding of the impact of spin fluctuations on the structural phase transitions

of iron through the magnetic/electronic free-energy difference (α - γ) or through the spin-lattice coupling (γ - δ).

In Sec. II we summarize the TB model for atom-atom, atom-spin, and spin-spin interactions. In Sec. III we present our approach to compute the vibrational contribution to the free energy by spin-space averaging (SSA) [8] and Hamiltonian Monte Carlo [10–13] with a comparison to experimental phonon spectra at elevated temperatures. In Sec. IV we summarize the computation of the magnetic/electronic contribution to the free energy by thermodynamic integration along the Bain path. The total effect of both contributions is presented and discussed in Sec. V, including a comparison to the experimentally observed phase-transition temperatures. We conclude our paper with a summary of the structural and magnetic/electronic contributions to the free energy and how their interplay determines the phase transitions of iron.

II. TIGHT-BINDING MODEL

A. Hamiltonian

In our tight-binding model, we assume that the motion of the atomic and magnetic degrees of freedom (DOFs) is one or more orders of magnitude slower than the hopping of electrons between atoms. A simple justification of this approximation would be that electronic hopping has a timescale of 10^{-15} s [14], which is much faster than the inverse phonon frequency and the spin wave frequency. As the fast electrons adiabatically follow the motions of the slow variables, i.e., the electronic structure corresponds to the atomic and magnetic configurations, the atomic and magnetic DOFs interact indirectly via the electronic structure in addition to their direct interactions. Since the direct ion-ion Coulomb interactions or magnetic dipole-dipole interactions couple only the atomic or magnetic DOFs in the lattice or magnetic subsystems, respectively, the indirect interaction via the electronic structure works as the only mechanism to couple the lattice and magnetic subsystems if spin-orbit coupling is neglected [15]. These DOFs and couplings can be fully represented by a magnetic TB Hamiltonian.

The magnetic moments in iron originate from the spin angular momenta of electrons; that is, the magnetic DOFs are inherent in the electronic subsystem. Therefore, it is not straightforward to define the slow magnetic DOFs. In tight binding, however, an elegant treatment is available in terms of the static-field approximation in the functional-integral formalism proposed by Hubbard [16,17]. Using this approximation, we derive a magnetic TB Hamiltonian that enables us to extract the slow magnetic DOFs, the local exchange fields, from the electronic subsystem. We present the key results in the following and give a detailed discussion in Appendix A. In our TB framework, the potential energy is a function of atomic positions $\mathbf{r}_1, \mathbf{r}_2, \dots, \mathbf{r}_N$ and local exchange fields $\mathbf{h}_1, \mathbf{h}_2, \dots, \mathbf{h}_N$,

$$E_{\text{pot}}(\{\mathbf{r}_i, \mathbf{h}_i\}) = E_{\text{band}}(\{\mathbf{r}_i, \mathbf{h}_i\}) + \sum_i \frac{1}{J_i} \mathbf{h}_i^2 - \frac{1}{2} \sum_i \left(U_i - \frac{1}{2} J_i \right) q_i^2 + E_{\text{pair}}(\{\mathbf{r}_i\}), \quad (3)$$

with N being the number of atoms in the supercell. J_i and U_i are the exchange parameter and the Coulomb parameter of atom i , and q_i is the atomic charge. The term E_{pair} is an empirical pairwise function of atomic positions that accounts for all the other contributions. E_{band} is the electronic band energy for the single-electron effective Hamiltonian

$$\hat{\mathcal{H}}_{\text{eff}} = \hat{\mathcal{H}}^{(0)} + 2 \sum_i \mathbf{h}_i \hat{\mathbf{S}}_i + \sum_i \mu_i \hat{\mathbf{n}}_i, \quad (4)$$

where $\hat{\mathbf{S}}_i$ is the spin operator at atom i that interacts with the local exchange field \mathbf{h}_i at the same atom and connects to the electronic structure via the occupation operators [see Eq. (A7)]. Similarly, the number operator $\hat{\mathbf{n}}_i$ interacts with the local Coulomb field μ_i . $\hat{\mathcal{H}}^{(0)}$ in Eq. (4) represents the Hamiltonian of the noninteracting electrons in the overlapping free-atom-like potentials. It is usually expressed in second quantization,

$$\hat{\mathcal{H}}^{(0)} = \sum_{\sigma} \sum_{i\alpha j\beta, i\alpha \neq j\beta} t_{i,j}^{\alpha\beta} \hat{c}_{i\alpha\sigma}^{\dagger} \hat{c}_{j\beta\sigma} + \sum_{i\alpha} E_{i\alpha}^0 \hat{\mathbf{n}}_{i\alpha}, \quad (5)$$

with $\hat{c}_{i\alpha\sigma}^{\dagger}$ ($\hat{c}_{i\beta\sigma}$) being the creation (annihilation) operator for the atomic orbital α (β) at atom i (j) in the spin- σ channel, $t_{i,j}^{\alpha\beta}$ being the hopping integral between the atomic orbital α of atom i and the atomic orbital β of atom j , $E_{i\alpha}^0$ being the on-site level of the free atom, and $\hat{\mathbf{n}}_{i\alpha}$ being the number operator for the atomic orbital α of atom i . The hopping integral $t_{i,j}^{\alpha\beta}$ is parameterized as a function of distance between atoms i and j within the two-center approximation [18]; that is, the influence of further atoms k on the interaction of atoms i and j is neglected.

With Eq. (3) we can define the magnetic partition function as an integral over spin space,

$$Z_{\text{mag}}(\{\mathbf{r}_i\}) = \int \prod_i d\mathbf{h}_i \exp[-\beta E_{\text{pot}}(\{\mathbf{r}_i, \mathbf{h}_i\})], \quad (6)$$

where we take into account both collinear and noncollinear magnetic excitations.

In our model, the magnetic and atomic subspaces are coupled via the band energy E_{band} in Eq. (3), which represents the electronic structure of a given atomic and magnetic configuration (see also the work by Drautz and Pettifor [15]). This coupling is the key difference between our model and those depending on classical or semiempirical spin-lattice coupling [4,19,20].

B. Computational details

The numerical TB calculations presented in the following were performed with the BOPfox program [21] using the method of Methfessel and Paxton [22] to sample the Brillouin zone. We use a parametrization of the TB Hamiltonian for Fe that was originally developed as a magnetic bond-order potential by Mrovec *et al.* [23]. This orthogonal d -valent model can also be evaluated within a TB framework and provides a robust description of the electronic and magnetic structure of iron. In particular, it captures important properties at $T = 0$ K like the phonon spectra of bcc and fcc iron (see the Supplemental Material of Ref. [23]) and complex deformations [24] as well as the magnetic phase transition of bcc iron at elevated temperature [25].

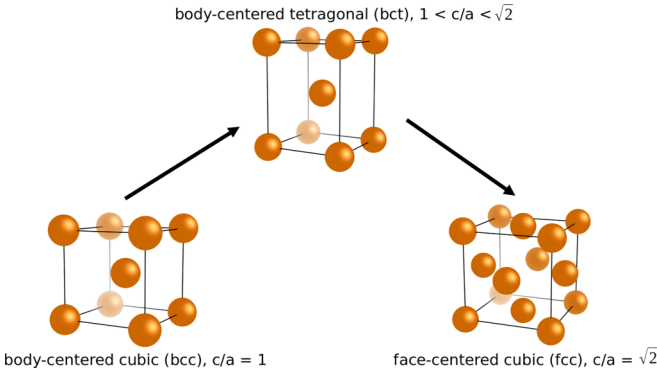


FIG. 1. Unit cells of the bct, bcc, and fcc lattices along the Bain path with the order parameter $k = c/a$.

The parameters $\bar{U} = U - 1/2J$ and J in Eq. (3) were chosen to be 3.6 and 0.8 eV, respectively, based on LDA + DMFT (LDA = local density approximation) calculations from Belozarov and Anisimov [26]. The thermal expansion is taken into account by interpolating/extrapolating the experimental lattice parameters of bcc and fcc iron measured at various temperatures [27].

The thermodynamic integration is carried out along the Bain path indicated in Fig. 1 as a simple model of a displacive structural phase transition between bcc and fcc. We use an order parameter k that refers to the c/a ratio of the body-centered tetragonal (bct) unit cell with $k = 1$ for bcc and $k = \sqrt{2}$ for fcc.

The influence of spin-orbit coupling is neglected in this work as the differences in the magnetic anisotropy energy (MAE) are expected to be less than 1 $\mu\text{eV}/\text{atom}$ for the cubic bcc and fcc lattices. Even MAE values along the Bain path of Fe of up to 0.1 meV/atom [28] are an order of magnitude smaller than the free-energy differences computed in the following.

III. VIBRATIONAL CONTRIBUTION TO THE PHASE TRANSITION

A. Thermal averaging in spin space

To take into account the effect of magnon-phonon coupling in the calculations of the vibrational free-energy difference, we employ the SSA scheme [8]. We note that classical spin vectors in the original SSA scheme are replaced by the local exchange fields in this work. Based on the approximation that magnetic excitations have a faster timescale than atomic vibrations, we can define the mean atomic force on atom i at finite temperature as

$$\bar{\mathbf{F}}_i = \frac{1}{Z_{\text{mag}}} \int \prod_i d\mathbf{h}_i \mathbf{F}_i(\{\mathbf{h}_i\}) \exp[-\beta E_{\text{pot}}(\{\mathbf{h}_i\})]. \quad (7)$$

The mean atomic force is then used together with the small-displacement scheme [29] to calculate the phonon densities of states of bcc and fcc iron at finite temperature, $g_{k=1}(\varepsilon, T)$ and $g_{k=\sqrt{2}}(\varepsilon, T)$, respectively. The phonon density of states becomes temperature dependent due to the thermal averaging in Eq. (7) for different magnetic temperatures at fixed atomic positions. The vibrational free-energy difference is evaluated

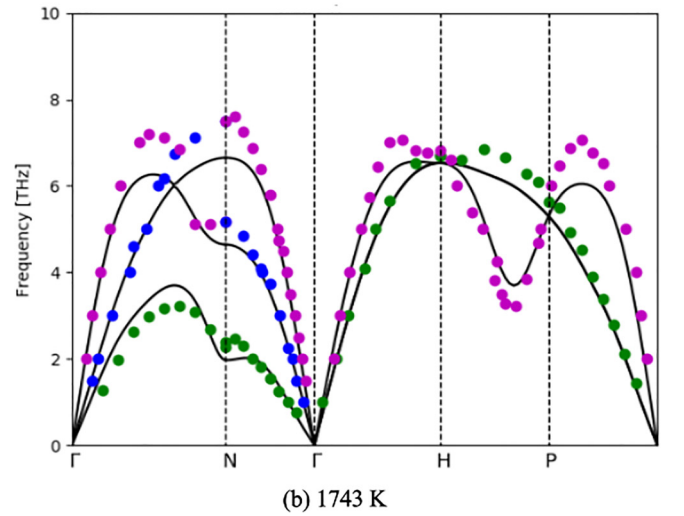
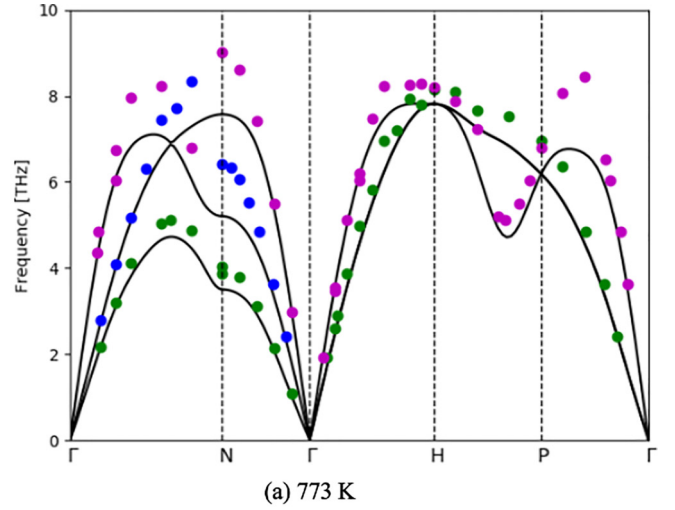


FIG. 2. Phonon spectrum of bcc iron at magnetic temperatures of (a) 773 and (b) 1743 K computed in this work (lines) and observed by experiment [30] (dots).

according to

$$\Delta F^{\text{vib}}(T) = \int_0^\infty F^{\text{ho}}(\varepsilon, T) [g_{k=\sqrt{2}}(\varepsilon, T) - g_{k=1}(\varepsilon, T)] d\varepsilon, \quad (8)$$

where $F^{\text{ho}}(\varepsilon, T)$ is the free energy at temperature T of the quantum harmonic oscillator,

$$F^{\text{ho}}(\varepsilon, T) = \frac{\varepsilon}{2} + \frac{1}{\beta} \ln[1 - \exp(-\beta\varepsilon)], \quad (9)$$

with an oscillation frequency of $\omega = \varepsilon/\hbar$. The thermal averages in spin space in Eq. (7) [and also in Eq. (15)] are computed numerically with the Hamiltonian Monte Carlo method as described in Appendix B.

B. Vibrational free-energy difference

Using spin-space averaging with the TB Hamiltonian for iron, we computed the phonon spectrum of bcc iron at different temperatures. In Fig. 2 we compare our results to the experimental phonon spectrum measured by Neuhaus

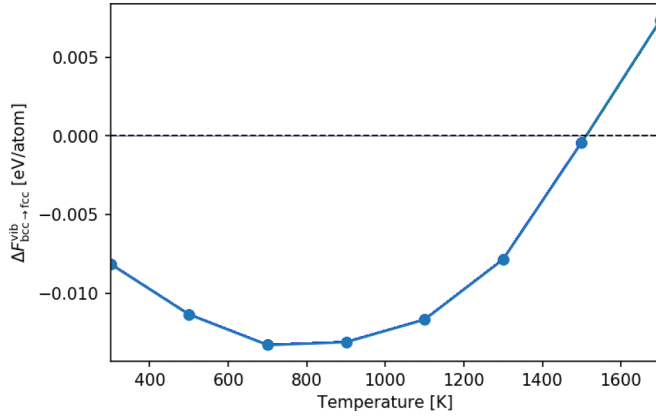


FIG. 3. Calculated vibrational free-energy difference between fcc and bcc phases of iron as a function of temperature obtained with SSA forces. Negative values correspond to stable fcc.

et al. [30] at 773 and 1743 K. We find good agreement with the experimental data for the considered temperatures given that we use a simple TB model that includes only d electrons. In particular, our calculations reproduce the strong phonon softening in bcc iron with increasing temperature. This effect was successfully captured earlier but only with DFT [5] or DFT+DMFT [6,7] methods that are much more sophisticated and computationally expensive than the tight-binding model used in this work. This confirms that our approach with an orthogonal, d -valent TB model and the chosen parametrization for iron is sufficient for a reliable treatment of iron at elevated temperatures.

From the phonon spectrum of bcc and fcc iron at different temperatures, $g_{k=1}(\varepsilon, T)$ and $g_{k=\sqrt{2}}(\varepsilon, T)$, we obtain the free-energy difference $\Delta F^{\text{vib}}(T)$ with Eq. (8). Our results in the temperature range of 300–1700 K are shown in Fig. 3. We find that the vibrational free-energy difference first decreases in the low-temperature range with increasing temperature and then starts to increase at around 700 K. It continues to increase with increasing temperature and changes from a negative value to a positive value at around 1500 K. This sign change indicates a structural phase transition from fcc to bcc at around 1500 K. As this phase transition is obtained by considering only $\Delta F^{\text{vib}}(T)$, we conclude that the vibrational contribution to the free energy from SSA forces stabilizes fcc iron for temperatures below 1500 K, while it tends to stabilize bcc iron at temperatures above 1500 K.

IV. MAGNETIC/ELECTRONIC CONTRIBUTION TO THE PHASE TRANSITION

A. Thermodynamic integration of the free-energy difference

The magnetic/electronic free-energy difference, ΔF^{elec} in Eq. (2), is computed by thermodynamic integration from bcc iron to fcc iron along the Bain path indicated in Fig. 1. With the order parameter k as the c/a ratio of the bct unit cell, we obtain

$$\Delta F^{\text{elec}} = \int_1^{\sqrt{2}} \frac{\partial F^{\text{elec}}}{\partial k} dk, \quad (10)$$

with the integral running from bcc ($k = 1$) to fcc ($k = \sqrt{2}$). Here we consider only the magnetic excitations described by the local exchange fields, i.e., $F^{\text{elec}} = -k_B T \ln(Z_{\text{mag}})$, where Z_{mag} is defined in Eq. (6). The derivative of the magnetic/electronic free energy with respect to the order parameter becomes a thermal average in the spin space,

$$\frac{\partial F^{\text{elec}}}{\partial k} = \left\langle \frac{\partial E_{\text{pot}}}{\partial k} \right\rangle. \quad (11)$$

We next show that this term can be expressed in terms of the stress tensor.

By writing the supercell at a given order parameter k along the volume-conserving Bain transformation as

$$\mathbf{C} = \begin{vmatrix} V^{\frac{1}{3}} k^{-\frac{1}{3}} & 0 & 0 \\ 0 & V^{\frac{1}{3}} k^{-\frac{1}{3}} & 0 \\ 0 & 0 & V^{\frac{1}{3}} k^{\frac{2}{3}} \end{vmatrix},$$

we can express an infinitesimal deformation of the supercell in terms of the order parameter k ,

$$\delta \mathbf{C} = \begin{vmatrix} -\frac{1}{3} V^{\frac{1}{3}} k^{-\frac{4}{3}} \delta k & 0 & 0 \\ 0 & -\frac{1}{3} V^{\frac{1}{3}} k^{-\frac{4}{3}} \delta k & 0 \\ 0 & 0 & \frac{2}{3} V^{\frac{1}{3}} k^{-\frac{1}{3}} \delta k \end{vmatrix}.$$

The infinitesimal deformation of the supercell can alternatively be expressed in terms of the strain tensor $\boldsymbol{\varepsilon}$ as

$$\delta \mathbf{C} = \boldsymbol{\varepsilon} \mathbf{C}, \quad (12)$$

which by substitution leads to

$$\frac{\boldsymbol{\varepsilon}}{\delta k} = \begin{vmatrix} -\frac{1}{3} k^{-1} & 0 & 0 \\ 0 & -\frac{1}{3} k^{-1} & 0 \\ 0 & 0 & \frac{2}{3} k^{-1} \end{vmatrix}.$$

With this we can write the derivative of the potential energy with respect to the order parameter k in terms of the strain tensor,

$$\begin{aligned} \frac{\partial E_{\text{pot}}}{\partial k} &= \sum_{\alpha, \beta} \frac{\partial E_{\text{pot}}}{\varepsilon_{\alpha\beta}} \frac{\varepsilon_{\alpha\beta}}{\partial k} \\ &= -\frac{1}{3k} V (\sigma_{11} + \sigma_{22} - 2\sigma_{33}), \end{aligned} \quad (13)$$

where in the last expression we used the relation

$$\frac{\partial E_{\text{pot}}}{\partial \varepsilon_{\alpha\beta}} = V \sigma_{\alpha\beta}. \quad (14)$$

Inserting Eq. (13) in Eq. (11), we obtain the derivative of the magnetic/electronic free energy with respect to the Bain-path order parameter k as

$$\begin{aligned} \frac{\partial F^{\text{elec}}}{\partial k} &= -\frac{V}{3k Z_{\text{mag}}(k)} \int \prod_i d\mathbf{h}_i [\sigma_{11}(k, \{\mathbf{h}_i\}) + \sigma_{22}(k, \{\mathbf{h}_i\}) \\ &\quad - 2\sigma_{33}(k, \{\mathbf{h}_i\})] \exp[-\beta E_{\text{pot}}(k, \{\mathbf{h}_i\})], \end{aligned} \quad (15)$$

where $Z_{\text{mag}}(k)$ represents the magnetic partition function at the given c/a ratio, V is the volume of the supercell, and σ_{11} , σ_{22} , and σ_{33} are the diagonal components of the stress tensor.

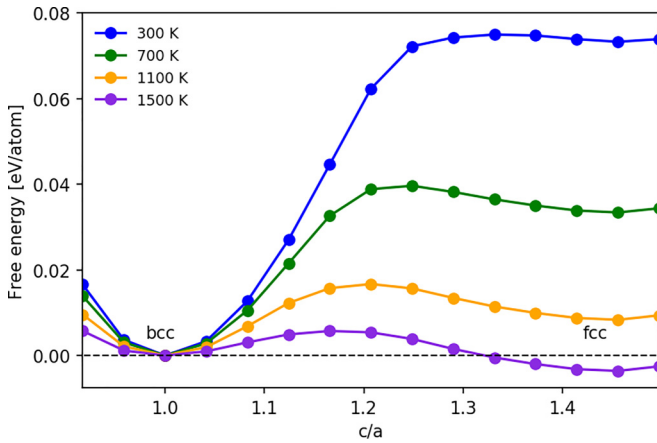


FIG. 4. Calculated magnetic/electronic free-energy profiles along the Bain path at different temperatures.

B. Magnetic/electronic free-energy difference

Using thermodynamic integration, we computed the magnetic/electronic contribution to the free-energy difference using the TB Hamiltonian and a $3 \times 3 \times 3$ bct supercell of iron containing 54 atoms. The large distance to the periodic images in this supercell provides a sufficient variety of the spin degrees of freedom for robust spin-space averaging. The resulting magnetic/electronic free-energy profiles along the Bain path are shown in Fig. 4 for temperatures of 300, 700, 1100, and 1500 K. We find that bcc iron is energetically most stable at low temperature compared to other c/a ratios. This is in line with the fact that bcc iron is the stable state of iron at low temperatures and pressures. With increasing temperature the spin fluctuations decrease the magnetic/electronic free-energy difference $F_{fcc}^{mag} - F_{bcc}^{mag}$ and reduce the barrier between bcc and fcc iron.

For the highest temperature in Fig. 4 the magnetic/electronic free-energy difference is negative, which marks a phase transition from bcc to fcc iron. By sampling the magnetic/electronic free-energy difference in the temperature range from 300 to 1700 K we can identify a phase-transition temperature of ≈ 1400 K, as shown in Fig. 5.

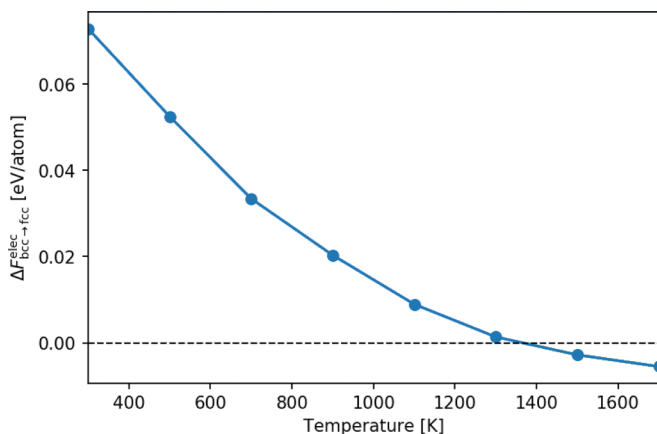


FIG. 5. Calculated magnetic/electronic free-energy difference between fcc and bcc phases of iron as a function of temperature.

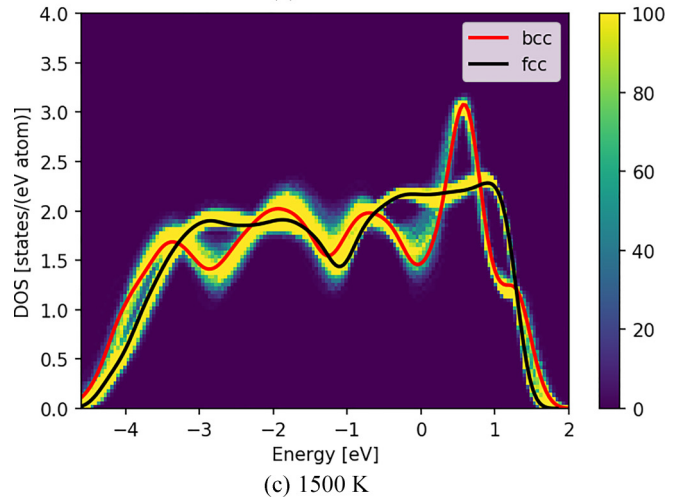
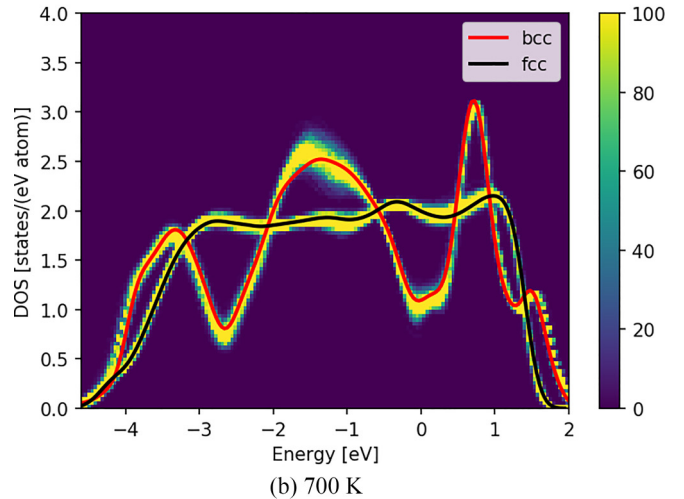
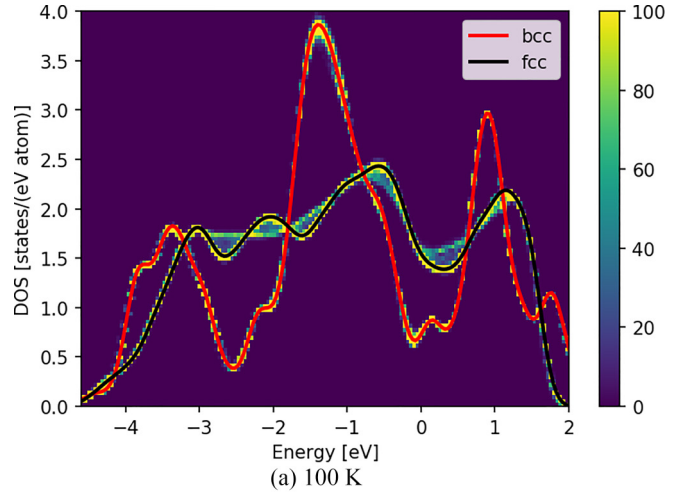


FIG. 6. Histograms of the electronic density of states of bcc and fcc iron at different magnetic temperatures. The electronic density of states of 1000 magnetic configurations were calculated at each temperature.

As we considered only $\Delta F^{elec}(T)$ here, we can conclude that the magnetic/electronic contribution to the free-energy difference tends to stabilize bcc iron for temperatures below 1400 K, while it tends to stabilize fcc iron at temperatures above 1400 K.

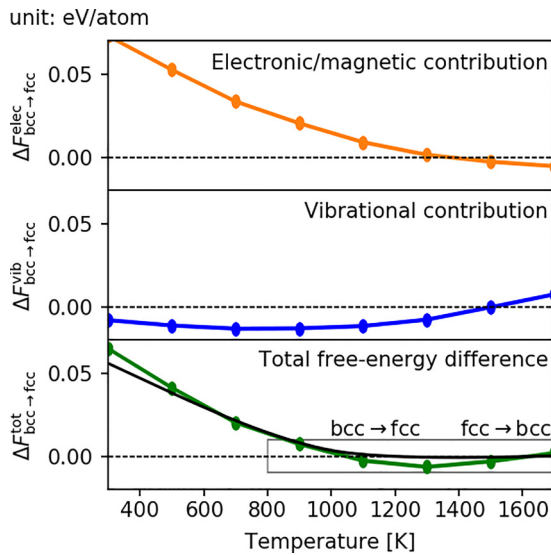


FIG. 7. Comparison of the electronic (orange), vibrational (blue), and total free-energy differences (green) between bcc and fcc iron plotted as a function of temperature. For comparison we also include CALPHAD calculations [32] with the SGTE database [33] (black). The gray box in the total free-energy difference panel is the zoom region for Fig. 8.

This structural phase transition from bcc to fcc can be understood in terms of the temperature-dependent change in the electronic structure due to spin fluctuations. In order to visualize this effect, we generate 1000 spin configurations by sampling spin space at different temperatures with Hamiltonian Monte Carlo. For each spin configuration, the electronic DOS is obtained numerically by a TB calculation. The DOSs of all spin configurations are combined for each temperature and plotted as a histogram in Fig. 6 for bcc and fcc iron at the different temperatures.

Comparing the different temperatures, we see that the influence of the spin fluctuation on the electronic DOS is considerably stronger for bcc iron than for fcc iron. This can be attributed to the collapse of magnetic ordering in bcc iron in the considered temperature range. Furthermore, the electronic DOSs of bcc and fcc iron are noticeably different at low temperature but become similar at high temperature. This explains why the magnetic/electronic contribution to the free-energy difference that is obtained by integrating the electronic DOS is small in the high-temperature regime. A similar result was reported by Alling *et al.* [31] based on DFT calculations. Besides magnetic excitations, the authors in that work also considered lattice vibrations and found that lattice vibrations can make the electronic DOSs of bcc and fcc iron even closer. Our observation is in line with the deduction based on experiments that the magnetic/electronic contribution is small in the γ (fcc)- δ (bcc) phase transition [30].

V. TOTAL FREE-ENERGY DIFFERENCE

The combined effects of the spin fluctuations on the free-energy difference are obtained by adding the vibrational contribution shown in Fig. 3 and the magnetic/electronic contribution shown in Fig. 5 to the total free-energy difference

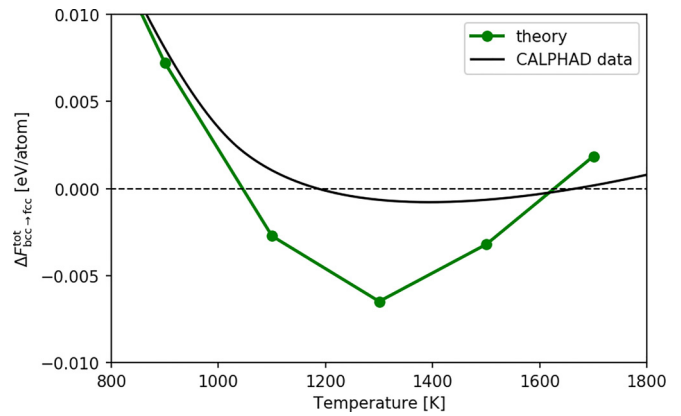


FIG. 8. Computed total free-energy difference near phase transitions (zoom of gray box in Fig. 7) and comparison to CALPHAD calculations [32] with the SGTE database [33].

shown in Fig. 7. A positive value $\Delta F^{\text{tot}}(T) > 0$ indicates a stable fcc structure, whereas a negative value $\Delta F^{\text{tot}}(T) < 0$ corresponds to a stable bcc structure.

For temperatures below ≈ 900 K, the gain of the exchange energy due to the ferromagnetic ordering significantly lowers the internal energy in bcc iron, and the magnetic/electronic contribution plays a dominant role for the total free-energy difference. At temperatures above ≈ 900 K, the magnetic/electronic contribution decreases to the same energy scale as the vibrational contribution, and the competition of the two contributions leads to the structural phase transitions α (bcc)- γ (fcc)- δ (bcc) that are observed in experiment. These findings show that the magnetic excitations alone can drive only the α (bcc)- γ (fcc) phase transition and not the γ (fcc)- δ (bcc) phase transition. The latter is mainly driven by vibrational excitations. Therefore, our work supports the findings based on disordered-local-moment (DLM) *ab initio* molecular dynamics [31], DFT+DMFT [2,6,34], and experiment [30].

We obtain a α (bcc)- γ (fcc) phase-transition temperature of around 1050 K and a γ (fcc)- δ (fcc) phase-transition temperature of around 1600 K. These results from our TB calculations are in good agreement with the corresponding experimental values [27] of 1189 K for and 1662 K. This is also visible in the good agreement with the results of CALPHAD calculations [32] shown in Fig. 8. The calculations were carried out using the Thermo-Calc software [35] with the SGTE database [33] that was optimized to reproduce experimental data in the whole temperature range.

VI. CONCLUSION

Iron changes its crystal structure from α (bcc) to γ (fcc) to δ (bcc) with increasing temperature. We applied a magnetic, orthogonal, d -valent TB model to clarify the influence of spin fluctuations on these structural phase transitions. The interplay between spin fluctuations and atomic vibrations was included by computing the effect of spin fluctuations on phonons using a spin-space-averaging scheme and spin-space sampling by Hamiltonian Monte Carlo. The magnetic/electronic contribution to the free energy was determined by thermodynamic integration along the Bain path between bcc and fcc. In this way we were able to compute the

temperature-dependent vibrational and magnetic/electronic contributions to the phase transitions of iron within a consistent framework at the TB level.

Our computed temperature-dependent vibrational and magnetic/electronic contributions to the free energy of bcc and fcc iron show that spin fluctuations influence the α - γ and γ - δ phase transitions via different mechanisms. The first mechanism, the influence of spin fluctuations on the magnetic free energy, decreases the free energy of bcc iron relative to that of fcc iron with increasing temperatures and impacts the α - γ phase transition. The second mechanism, the spin-lattice coupling, increases the free energy of bcc iron relative to that of fcc iron and impacts the γ - δ phase transition.

By adding the vibrational and magnetic/electronic contributions to the free-energy difference we can reproduce the experimentally observed sequence of structural phase transitions. In the low-temperature regime ($T < 900$ K), the difference of the magnetic/electronic contribution between the phases plays the dominant role and is much larger than the difference of the vibrational contribution. In this region bcc iron is stabilized by the large exchange-energy gain of the ferromagnetic ordering. In the high-temperature range ($T > 900$ K), the difference of the magnetic/electronic contribution decreases to the same energy scale as the difference of the vibrational contribution due to the loss of ferromagnetic ordering in bcc iron. In this temperature range, the difference of the magnetic/electronic contribution decreases from a positive to a negative value, while the difference of the vibrational contribution increases from a negative to a positive value. This competition leads to the α (bcc) to γ (fcc) to δ (bcc) phase transition in iron.

Our framework with a magnetic TB Hamiltonian can hence explain the microscopic origin of the structural phase transitions in iron. The sequence of phase transitions is correctly captured with phase-transition temperatures of around 1050 and 1600 K, in good agreement with experiment.

ACKNOWLEDGMENTS

We acknowledge financial support from the International Max Planck Research School SurMat. J.R. acknowledges financial support from the German Research Foundation (DFG) through the DFG Heisenberg Programme, Project No. 428315600.

APPENDIX A: DERIVATION OF THE MAGNETIC HAMILTONIAN

In the following, we give a formal derivation of the magnetic Hamiltonian given in Sec. II A. In principle, the many-electron system can be accurately described by the Hamiltonian below in second quantization [36]:

$$\begin{aligned}\hat{H} &= \hat{H}^{(0)} + \hat{V}, \\ \hat{V} &= \frac{1}{2} \sum_{\sigma\sigma'} \sum_{il} \sum_{i'l'} \sum_{mm'} \sum_{pp'} V_{ill'i'}^{mpp'm'} \hat{c}_{im\sigma}^\dagger \hat{c}_{lp\sigma'}^\dagger \hat{c}_{l'p'\sigma'} \hat{c}_{i'm'\sigma}, \\ V_{ill'i'}^{mpp'm'} &= e^2 \iint d\mathbf{r} d\mathbf{r}' \frac{1}{|\mathbf{r} - \mathbf{r}'|} W_m(\mathbf{r} - \mathbf{R}_i) W_p(\mathbf{r}' - \mathbf{R}_l) \\ &\quad \times W_{p'}(\mathbf{r}' - \mathbf{R}_{l'}) W_{m'}(\mathbf{r} - \mathbf{R}_{i'}),\end{aligned}\quad (\text{A1})$$

where $\hat{H}^{(0)}$ is the noninteracting part of the Hamiltonian that contains no electron-electron interactions and \hat{V} is the interaction Hamiltonian that describes electron-electron interactions. $W_m(\mathbf{r} - \mathbf{R}_i)$ represents the m th Wannier orbital at site i . In our work, we replace the Wannier-orbital basis by the orthogonal atomic-orbital basis and denote this treatment as tight-binding approximation.

The interaction Hamiltonian \hat{V} contains both interatomic and intra-atomic contributions. If we neglect the interatomic contributions and consider only intra-atomic electron-electron interactions, the interaction Hamiltonian \hat{V} is simplified [36]:

$$\begin{aligned}\hat{V} &\approx \frac{1}{2} \sum_i \sum_{\sigma} \left\{ \sum_{mm'} U_{i,mm'} \hat{n}_{im\sigma} \hat{n}_{im'-\sigma} \right. \\ &\quad + \sum_{m \neq m'} [(U_{i,mm'} - J_{i,mm'}) \hat{n}_{im\sigma} \hat{n}_{im'\sigma} \\ &\quad \left. - J_{i,mm'} c_{im\sigma}^\dagger c_{im-\sigma} c_{im'-\sigma}^\dagger c_{im'\sigma}] \right\}.\end{aligned}\quad (\text{A2})$$

$U_{i,mm'}$ and $J_{i,mm'}$ are the Coulomb and exchange integrals and are defined as

$$\begin{aligned}U_{i,mm'} &= V_{iiii}^{mm'm'm}, \\ J_{i,mm'} &= V_{iiii}^{mm'mm'}.\end{aligned}\quad (\text{A3})$$

The orbital-resolved Coulomb and exchange integrals in Eq. (A2) are difficult to handle. A frequently used simplification is to replace $U_{i,mm'}$ and $J_{i,mm'}$ by their average values U_i and J_i and to simplify the interaction Hamiltonian as

$$\begin{aligned}\hat{V} &\approx \frac{1}{2} \sum_i \sum_{m,m'} \sum_{\sigma} U_i \hat{n}_{im\sigma} \hat{n}_{im'-\sigma} \\ &\quad + \frac{1}{2} \sum_i \sum_{m \neq m'} \sum_{\sigma} (U_i - J_i) \hat{n}_{im\sigma} \hat{n}_{im'\sigma} \\ &\quad - \frac{1}{2} \sum_i \sum_{m \neq m'} \sum_{\sigma} J_i \hat{c}_{im\sigma}^\dagger \hat{c}_{im-\sigma} \hat{c}_{im'-\sigma}^\dagger \hat{c}_{im'\sigma}.\end{aligned}\quad (\text{A4})$$

A further simplification is to drop out the last term in Eq. (A4) within the diagonal density approximation [37]. Then the interaction Hamiltonian becomes

$$\begin{aligned}\hat{V} &\approx \frac{1}{2} \sum_i \sum_{m,m'} \sum_{\sigma} U_i \hat{n}_{im\sigma} \hat{n}_{im'-\sigma} \\ &\quad + \frac{1}{2} \sum_i \sum_{m \neq m'} \sum_{\sigma} (U_i - J_i) \hat{n}_{im\sigma} \hat{n}_{im'\sigma} \\ &\equiv \frac{1}{2} \sum_{i\sigma} U_i \hat{n}_{i\sigma} \hat{n}_{i-\sigma} + \frac{1}{2} \sum_{i\sigma} (U_i - J_i) \hat{n}_{i\sigma} \hat{n}_{i\sigma} \\ &\quad - \frac{1}{2} \sum_{im\sigma} (U_i - J_i) \hat{n}_{im\sigma},\end{aligned}\quad (\text{A5})$$

where we employed the identities below from the first to the second line on the right-hand side,

$$\begin{aligned}\hat{n}_{i\sigma} &= \sum_m \hat{n}_{im\sigma}, \\ (\hat{n}_{im\sigma})^2 &= \hat{n}_{im\sigma}.\end{aligned}\quad (\text{A6})$$

The second identity is valid due to the Pauli principle.

We next choose the quantization axis at site i along a chosen direction \mathbf{e}_i and use the identities

$$\begin{aligned}\mathbf{e}_i \hat{\mathbf{S}}_i &= \frac{1}{2}(\hat{n}_{i\uparrow} - \hat{n}_{i\downarrow}), \\ \hat{n}_i &= \hat{n}_{i\uparrow} + \hat{n}_{i\downarrow}\end{aligned}\quad (\text{A7})$$

to reformulate the interaction Hamiltonian (A5) as

$$\begin{aligned}\hat{V} &\approx \frac{1}{2} \sum_i \left(U_i - \frac{1}{2} J_i \right) (\hat{n}_i)^2 - \sum_i J_i (\mathbf{e}_i \hat{\mathbf{S}}_i)^2 \\ &\quad - \frac{1}{2} \sum_{i\sigma} (U_i - J_i) \hat{n}_{i\sigma} \\ &\equiv \frac{1}{2} \sum_i \bar{U}_i (\hat{n}_i)^2 - \sum_i J_i (\mathbf{e}_i \hat{\mathbf{S}}_i)^2 - \frac{1}{2} \sum_{i\sigma} (U_i - J_i) \hat{n}_{i\sigma}.\end{aligned}\quad (\text{A8})$$

Here we introduced the spin operator $\hat{\mathbf{S}}_i$ and the new parameter $\bar{U}_i = U_i - \frac{1}{2} J_i$. The last term does not contain quadratic contributions, and from now on we group it into the noninteracting-electron Hamiltonian $\hat{\mathcal{H}}^{(0)}$. We obtain a simplified many-electron Hamiltonian:

$$\hat{\mathcal{H}} \approx \hat{\mathcal{H}}^{(0)} - \sum_i J_i (\mathbf{e}_i \hat{\mathbf{S}}_i)^2 + \frac{1}{2} \sum_i \bar{U}_i (\hat{n}_i)^2, \quad (\text{A9})$$

where the last term corresponds to a quantized treatment of the Coulomb interaction that is replaced by a mean-field treatment in our model. We fully follow the approximations introduced by Hubbard [16,17] to treat the second term. The treatments based on the Hubbard-Stratonovich transformation and the static approximation were discussed in detail in his original papers and also shown in [38], which leads to the tight-binding model in this work.

APPENDIX B: HAMILTONIAN MONTE CARLO

Hamiltonian Monte Carlo (HMC) combines Monte Carlo and molecular dynamics and has proven to be an efficient method to sample complex energy landscapes [10–13].

In this paper, we employ HMC to sample the spin space $\{\mathbf{h}_1, \mathbf{h}_2, \dots, \mathbf{h}_N\}$. The local exchange field \mathbf{h}_i here is a three-dimensional vector, different from the unit spin vector in our previous work [25]. It allows us to employ conventional molecular dynamics to generate proposal states in HMC, as compared to the auxiliary spin dynamics in [25].

In our HMC implementation we first introduce an auxiliary momentum variable \mathbf{p}_i for every local exchange field \mathbf{h}_i . The auxiliary momentum variables $\mathbf{p}_1, \mathbf{p}_2, \dots, \mathbf{p}_N$ and the local exchange fields $\mathbf{h}_1, \mathbf{h}_2, \dots, \mathbf{h}_N$ together define a state X in phase space. We then define the auxiliary Hamiltonian as

$$H(X) = \sum_{i=1}^N \frac{\mathbf{p}_i^2}{2m} + E_{\text{pot}}(\{\mathbf{h}_i\}), \quad (\text{B1})$$

with the potential energy E_{pot} defined in Eq. (3) and the auxiliary mass m required in HMC. The HMC trajectory is then generated by the following procedure:

(i) Starting from a current state X_I , perform a Gibbs sampling for the momentum variables and generate a new state \bar{X}_I by randomly choosing new values of the momentum variables \mathbf{p}_i according to their Gaussian distribution,

$$\rho(\mathbf{p}_1, \dots, \mathbf{p}_N) = \prod_{i=1}^N \left(\frac{\beta}{2\pi m} \right)^{3/2} \exp \left\{ -\beta \sum_{i=1}^N \frac{\mathbf{p}_i^2}{2m} \right\}. \quad (\text{B2})$$

(ii) Run molecular dynamics for a trajectory length L from the initial state $X^{\text{HD}}(0)$ chosen as \bar{X}_I using the equations of motion for Hamiltonian dynamics

$$\begin{aligned}\frac{d\mathbf{h}_i}{dt} &= \frac{\mathbf{p}_i}{m_i}, \\ \frac{d\mathbf{p}_i}{dt} &= -\frac{\partial E_{\text{pot}}}{\partial \mathbf{h}_i}.\end{aligned}\quad (\text{B3})$$

The final state of the molecular-dynamics trajectory is denoted as $X^{\text{HD}}(L)$.

(iii) Negate the momentum variables of $X^{\text{HD}}(L)$ to obtain the proposed state \bar{X}_{I+1} for a Metropolis update. Discarding the momentum part results in a deterministic generation $\bar{X}_I \rightarrow \bar{X}_{I+1}$ and is necessary to obtain a symmetric generation probability.

(iv) Calculate the Metropolis acceptance ratio

$$p(\bar{X}_I \rightarrow \bar{X}_{I+1}) = \min\{1, e^{[\beta H(\bar{X}_I) - \beta H(\bar{X}_{I+1})]}\}, \quad (\text{B4})$$

and accept the proposed state \bar{X}_{I+1} as the next state X_{I+1} of the Markov chain with the probability p .

(v) Repeat the steps above to generate a Markov chain.

[1] H. Hasegawa and D. G. Pettifor, *Phys. Rev. Lett.* **50**, 130 (1983).
 [2] I. Leonov, A. I. Poteryaev, V. I. Anisimov, and D. Vollhardt, *Phys. Rev. Lett.* **106**, 106405 (2011).
 [3] F. Körmann, T. Hickel, and J. Neugebauer, *Curr. Opin. Solid State Mater. Sci.* **20**, 77 (2016).
 [4] P. W. Ma, S. L. Dudarev, and J. S. Wróbel, *Phys. Rev. B* **96**, 094418 (2017).
 [5] F. Körmann, B. Grabowski, B. Dutta, T. Hickel, L. Mauger, B. Fultz, and J. Neugebauer, *Phys. Rev. Lett.* **113**, 165503 (2014).

[6] I. Leonov, A. I. Poteryaev, Y. N. Gornostyrev, A. I. Lichtenstein, M. I. Katsnelson, V. I. Anisimov, and D. Vollhardt, *Sci. Rep.* **4**, 5585 (2014).
 [7] Q. Han, T. Birol, and K. Haule, *Phys. Rev. Lett.* **120**, 187203 (2018).
 [8] F. Körmann, A. Dick, B. Grabowski, T. Hickel, and J. Neugebauer, *Phys. Rev. B* **85**, 125104 (2012).
 [9] L. Mauger, M. S. Lucas, J. A. Muñoz, S. J. Tracy, M. Kresch, Y. Xiao, P. Chow, and B. Fultz, *Phys. Rev. B* **90**, 064303 (2014).

- [10] S. Duane, A. Kennedy, B. J. Pendleton, and D. Roweth, *Phys. Lett. B* **195**, 216 (1987).
- [11] R. M. Neal, in *Handbook of Markov Chain Monte Carlo*, edited by S. Brooks, A. Gelman, G. L. Jones, and X. Meng (CRC Press, Boca Raton, FL, 2011), Chap. 5, pp. 113–162.
- [12] M. Betancourt, S. Byrne, S. Livingstone, and M. Girolami, *Bernoulli* **23**, 2257 (2017).
- [13] M. Betancourt, [arXiv:1701.02434](https://arxiv.org/abs/1701.02434).
- [14] B. L. Gyorffy, A. J. Pindor, J. Staunton, G. M. Stocks, and H. Winter, *J. Phys. F* **15**, 1337 (1985).
- [15] R. Drautz and D. G. Pettifor, *Phys. Rev. B* **84**, 214114 (2011).
- [16] J. Hubbard, *Phys. Rev. B* **20**, 2626 (1979).
- [17] J. Hubbard, *Phys. Rev. B* **20**, 4584 (1979).
- [18] J. C. Slater, *Phys. Rev.* **49**, 537 (1936).
- [19] P. W. Ma, C. H. Woo, and S. L. Dudarev, *Phys. Rev. B* **78**, 024434 (2008).
- [20] J. Hellsvik, D. Thonig, K. Modin, D. Iuşan, A. Bergman, O. Eriksson, L. Bergqvist, and A. Delin, *Phys. Rev. B* **99**, 104302 (2019).
- [21] T. Hammerschmidt, B. Seiser, M. E. Ford, A. N. Ladines, S. Schreiber, N. Wang, J. Jenke, Y. Lysogorskiy, C. Teijeiro, M. Mrovec, M. Cak, E. R. Margine, D. G. Pettifor, and R. Drautz, *Comput. Phys. Commun.* **235**, 221 (2019).
- [22] M. Methfessel and A. T. Paxton, *Phys. Rev. B* **40**, 3616 (1989).
- [23] M. Mrovec, D. Nguyen-Manh, C. Elsässer, and P. Gumbsch, *Phys. Rev. Lett.* **106**, 246402 (2011).
- [24] J. J. Möller, M. Mrovec, I. Bleskov, J. Neugebauer, T. Hammerschmidt, R. Drautz, C. Elsässer, T. Hickel, and E. Bitzek, *Phys. Rev. Mater.* **2**, 093606 (2018).
- [25] N. Wang, T. Hammerschmidt, J. Rogal, and R. Drautz, *Phys. Rev. B* **99**, 094402 (2019).
- [26] A. S. Belozero and V. I. Anisimov, *J. Phys.: Condens. Matter* **26**, 375601 (2014).
- [27] Z. S. Basinski, W. Hume-Rothery, and A. L. Sutton, *Proc. R. Soc. London, Ser. A* **229**, 459 (1955).
- [28] T. Burkert, O. Eriksson, P. James, S. I. Simak, B. Johansson, and L. Nordström, *Phys. Rev. B* **69**, 104426 (2004).
- [29] A. Togo and I. Tanaka, *Scr. Mater.* **108**, 1 (2015).
- [30] J. Neuhaus, M. Leitner, K. Nicolaus, W. Petry, B. Hennion, and A. Hiess, *Phys. Rev. B* **89**, 184302 (2014).
- [31] B. Alling, F. Körmann, B. Grabowski, A. Glensk, I. A. Abrikosov, and J. Neugebauer, *Phys. Rev. B* **93**, 224411 (2016).
- [32] F. Körmann (private communication).
- [33] A. Dinsdale, *CALPHAD: Comput. Coupling Phase Diagrams Thermochem.* **15**, 317 (1991).
- [34] A. A. Katanin, A. S. Belozero, and V. I. Anisimov, *Phys. Rev. B* **94**, 161117(R) (2016).
- [35] J. Andersson, T. Helander, L. Höglund, P. Shi, and B. Sundman, *CALPHAD: Comput. Coupling Phase Diagrams Thermochem.* **26**, 273 (2002).
- [36] T. Moriya, *Spin Fluctuations in Itinerant Electron Magnetism*, Springer Series in Solid-State Sciences (Springer, Berlin, 1985).
- [37] M. I. Katsnelson and A. I. Lichtenstein, *Phys. Rev. B* **61**, 8906 (2000).
- [38] N. Wang, Ph.D. thesis, Ruhr-Universität Bochum, 2019, <https://hss-opus.ub.ruhr-uni-bochum.de/opus4/files/7138/diss.pdf>.